Appl. Math. Mech. -Engl. Ed., **44**(11), 1871–1886 (2023)

APPLIED MATHEMATICS AND MECHANICS (ENGLISH EDITION)

https://doi.org/10.1007/s10483-023-3051-6

Geometrically nonlinear inerter for vibration suppression*

Yuyang SONG[1], Liqun CHEN[2], Tianzhi YANG[1,†]

1. School of Mechanical Engineering and Automation, Northeastern University, Shenyang 110819, China;

2. Shanghai Institute of Applied Mathematics and Mechanics, Shanghai Key Laboratory of Mechanics in Energy Engineering, Shanghai Frontier Science Center of Mechanoinformatics, School of Mechanics and Engineering Science, Shanghai University, Shanghai 200444, China

(Received Jun. 16, 2023 / Revised Sept. 13, 2023)

Abstract A two-degree-of-freedom (2DOF) vibration isolation structure with an integrated geometric nonlinear inerter (NI) device is proposed. The device is integrated into an inertial nonlinear energy sink (INES), and its vibration suppression performance is examined by the Runge-Kutta (RK) method and verified by the harmonic balance method (HBM). The new isolator is compared with a traditional vibration isolator. The results show a significant improvement in the vibration suppression performance. To investigate the effects of the excitation amplitude and initial condition on the dynamics of the system, a series of transmissibility-frequency response analyses are performed based on the displacement transmissibility. The energy flow of the system is analyzed, and numerous calculations reveal a series of ideal values for the energy sink in the NI-INES system. This study provides new insights for the design of vibration isolators.

Key words inerter, nonlinear dynamic, isolator, energy

Chinese Library Classification O322
2010 Mathematics Subject Classification 34A34, 74H45

1 Introduction

Vibration isolators are widely used in the field of engineering. Vibrations are harmful to the human body[1]. When the vibration frequency is close to the frequency of human organs, it can cause discomfort in the body. Therefore, vibration isolation[2–4] technology plays a crucial role in ensuring comfort and safety. Housner et al.[5] and Tigli[6] formed a tuned mass damper (TMD) for improved vibration suppression by adding damping to the additional mass. However, the effective working bandwidth of the TMD is narrow. Igusa and Xu[7] and Zuo and Nayfeh[8] expanded the working bandwidth of linear vibration isolators by increasing the number of TMDs to form multiple TMDs, which improved the reliability of isolators and expanded their

* Citation: SONG, Y. Y., CHEN, L. Q., and YANG, T. Z. Geometrically nonlinear inerter for vibration suppression. *Applied Mathematics and Mechanics* (*English Edition*), **44**(11), 1871–1886 (2023) https://doi.org/10.1007/s10483-023-3051-6

† Corresponding author, E-mail: yangtianzhi@me.neu.edu.cn

Project supported by the National Natural Science Foundation of China (Nos. 12232014 and 12072221) and the Fundamental Research Funds for the Central Universities of China (No. 2013017)

applications. In addition, Nagashima and Shinozaki[9] and Loh and Lin[10] studied active tuned mass dampers (ATMDs). All of the studies mentioned above focused on linear isolators[11].

Carrella et al.[12] proposed that linear vibration isolators had a limited bandwidth for effective vibration isolation. The effectiveness of a vibration isolator in reducing vibrations decreases when strong nonlinear vibrations occur. To address this issue, Roberson[13] proposed incorporating nonlinear devices into linear vibration isolators. At present, the two most effective types of nonlinear isolators are quasi-zero stiffness isolators[14–15] and isolators with nonlinear energy sinks (NESs)[16–19]. Lu et al.[20–21] introduced a two-stage nonlinear vibration isolator that had superior isolation performance compared with linear isolator. In the NES, energy could be pumped unidirectionally into additional structures[22–24]. Zang et al.[25] introduced a lever structure, which achieved a good vibration suppression effect even with a small additional mass. Geng et al.[26] improved the energy absorption capacity of NES by using a piecewise spring device. Dang et al.[27] proposed a more efficient vibration reducer, which used the unidirectional force from ropes to make energy irreversibly flow into energy sinks. Savadkoohi et al.[28], Lamarque et al.[29], and Georgiadis et al.[30] proposed a non-smooth NES, and studied the target energy transfer (TET). Presently, nonlinear vibration isolators are used in various engineering fields such as construction[31–33], machine tools[34–35], aircrafts[36–38], pipelines[39], flywheels[40], beams[41–42], and energy harvesting[43–47].

Smith[48] proposed the concept of inerter, which was an inertial component that could provide large inertia with a small mass. Lazar et al.[49] proposed the use of an inerter-based device to reduce the vibration in civil engineering structures. Kuhnert et al.[50] reviewed the history of inerter's development. This type of inerter, such as ballscrew[51] and fluid[52] inerters, is important for the weight reduction of the vibration isolator. Zhang et al.[53] proposed to use an inerter instead of mass in the NES, and the present paper is also inspired by their work. In the field of nonlinear dynamics[54], nonlinear inerters (NIs) are also gaining attention. With reference to the nonlinear damping arrangement proposed in Ref. [55], inerters can also adopt similar arrangements. Moraes et al.[56] and Yang et al.[57] found that NIs might have a beneficial effect on high-frequency systems and could soften the stiffness. Dang et al.[58] proposed a dual-stage inerter-enhanced NES. Dong et al.[59] developed a joint device with an NI. In Ref. [60], the authors proposed the idea of placing the inerter in a quadrilateral structure, and an NI arrangement is also utilized in this paper.

The NI-inertial nonlinear energy sink (INES) uses an inerter instead of the mass element in the traditional NES structure and a geometric NI integrated into the inertial nonlinear energy sink for superior vibration isolation. This paper is organized as follows. In Section 2, a schematic diagram of the proposed structure is presented, and a dynamic model is developed. In Section 3, numerical simulations with the Runge-Kutta (RK) method are validated against the harmonic balance method (HBM), demonstrating the accuracy of the results. In Section 4, the vibration suppression performance of the proposed system is evaluated, and multiple sets of data are subjected to the dynamic analysis. In Section 5, the absorption efficiency of the energy sink in the vibration suppression system is investigated, and the optimal parameter range is provided. Finally, the obtained conclusions are presented in Section 6.

2 NI-INES system and modeling

The NI-INES is presented in Fig. 1(a). The spring k_1 and the damping c_1 connect the primary mass M to the ground. Below the main mass, the damping c_2 and the nonlinear stiffness k_2 are linked to three inerters by a T-shaped mechanism. The inerter has an inertia coefficient b, with one end attached to the T-shaped mechanism and the other end grounded. The other pair of inerters are horizontally arranged, with one end connected to the T-shaped mechanism and the other end connected separately to the main mass, and their inertia coefficients are $b/2$. The horizontally arranged inerters are shown in Fig. 1(b).

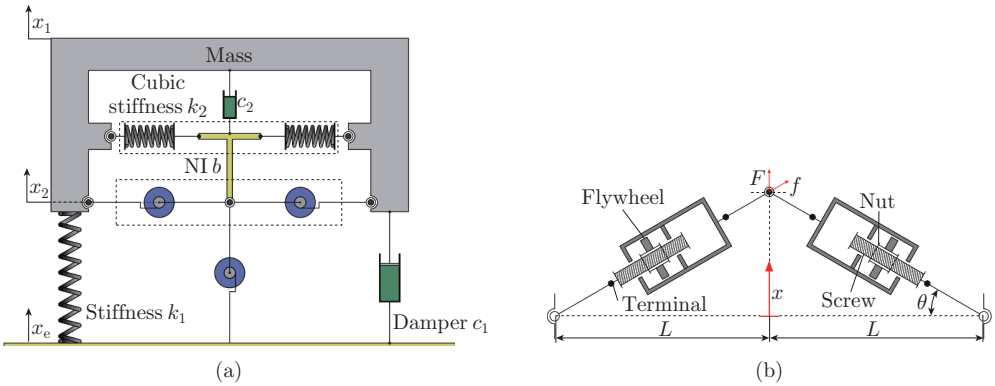

Fig. 1 (a) NI-INES system and (b) NI model (color online)

The NI is subjected to a force analysis. As it is shown in Fig. 1(b), the two terminals of inerters are connected by a hinge, while the other two ends are fixed. The force in the vertical direction is $F = 2f\sin\theta$, and the force along the inerter direction is

$$f = \frac{b}{2}\frac{\mathrm{d}(\dot{x}\sin\theta)}{\mathrm{d}\tau} = \frac{b}{2}\Big(\ddot{x}\sin\theta + \frac{\dot{x}^2L^2}{(L^2+x^2)(\sqrt{L^2+x^2})}\Big),$$

where

$$\sin\theta = \frac{x}{\sqrt{L^2+x^2}}.$$

Substituting each component into the F equation yields

$$F = b\Big(\frac{x^2\ddot{x}}{L^2+x^2} + \frac{L^2x\dot{x}^2}{(L^2+x^2)^2}\Big). \tag{1}$$

The Taylor expansion at $x = 0$ yields

$$F = b\Big(\frac{x^2\ddot{x}}{L^2} + \dot{x}^2x\Big(\frac{1}{L^2} - \frac{2x^2}{L^4}\Big)\Big). \tag{2}$$

The dynamic equations of the NI-INES system are shown as follows:

$$\begin{aligned} m\ddot{x}_1 = {} & -k_1(x_1 - x_e) - c_1(\dot{x}_1 - \dot{x}_e) - k_2(x_1 - x_2)^3 \\ & - c_2(\dot{x}_1 - \dot{x}_2) - b\Big((\ddot{x}_1 - \ddot{x}_2)\frac{(x_1 - x_2)^2}{L^2} \\ & + (\dot{x}_1 - \dot{x}_2)^2(x_1 - x_2)\Big(\frac{1}{L^2} - \frac{2(x_1 - x_2)^2}{L^4}\Big)\Big), \end{aligned} \tag{3}$$

$$\begin{aligned} b(\ddot{x}_2 - \ddot{x}_e) = {} & k_2(x_1 - x_2)^3 + c_2(\dot{x}_1 - \dot{x}_2) + b\Big((\ddot{x}_1 - \ddot{x}_2)\frac{(x_1 - x_2)^2}{L^2} \\ & + (\dot{x}_1 - \dot{x}_2)^2(x_1 - x_2)\Big(\frac{1}{L^2} - \frac{2(x_1 - x_2)^2}{L^4}\Big)\Big). \end{aligned} \tag{4}$$

The dimensionless equations can be derived as follows:

$$\begin{aligned} \ddot{x}_1 = {} & -(x_1 - x_e) - 2\zeta_1(\dot{x}_1 - \dot{x}_e) - \kappa(x_1 - x_2)^3 - 2\zeta_2(\dot{x}_1 - \dot{x}_2) \\ & - \mu\Big((\ddot{x}_1 - \ddot{x}_2)\frac{(x_1 - x_2)^2}{L^2} + (\dot{x}_1 - \dot{x}_2)^2(x_1 - x_2)\Big(\frac{1}{L^2} - \frac{2(x_1 - x_2)^2}{L^4}\Big)\Big), \end{aligned} \tag{5}$$

$$\ddot{x}_2 = \ddot{x}_{\mathrm{e}} + \frac{\kappa}{\mu}(x_1 - x_2)^3 + \frac{2\zeta_2}{\mu}(\dot{x}_1 - \dot{x}_2) + \Big((\ddot{x}_1 - \ddot{x}_2)\frac{(x_1 - x_2)^2}{L^2} + (\dot{x}_1 - \dot{x}_2)^2(x_1 - x_2)\Big(\frac{1}{L^2} - \frac{2(x_1 - x_2)^2}{L^4}\Big)\Big), \tag{6}$$

where

$$\begin{cases} \omega_0 = \sqrt{\dfrac{k_1}{m}}, \quad \zeta_1 = \dfrac{c_1}{2m\omega_0}, \quad \zeta_2 = \dfrac{c_2}{2m\omega_0}, \quad \kappa = \dfrac{k_2}{k_1}, \\ \mu = \dfrac{b}{m}, \quad \Omega = \dfrac{\omega}{\omega_0}, \quad t = \omega_0\tau, \quad T = \dfrac{R_{\mathrm{MS}}(x)}{R_{\mathrm{MS}}(A)}. \end{cases}$$

In the above equations, ω_0 is the natural frequency of the main mass, ζ is the damping ratio, κ is the stiffness ratio, μ is the ratio of the inertial coefficient to the main mass, Ω is the ratio of the excitation frequency to the natural frequency, and t is the non-dimensional time. T is the ratio of the root mean square displacement $R_{\mathrm{MS}}(x)$ to the root mean square input $R_{\mathrm{MS}}(A)$, which is defined as transmissibility.

3 Analytical method and numerical validation

The first-order HBM is used in this analysis with an external excitation of $x_{\mathrm{e}} = A\cos(\Omega t)$. Assumptions are made about the solutions for x_1 and x_2 as follows:

$$x_1 = a_1\cos(\Omega t) + b_1\sin(\Omega t), \quad x_2 = a_2\cos(\Omega t) + b_2\sin(\Omega t). \tag{7}$$

Substitute Eq. (7) into Eqs. (5) and (6). The two equations are treated with a trigonometric transformation that preserves the first harmonic term in both equations.

$$\begin{cases} F_1(a_1, b_1, a_2, b_2, \Omega)\cos(\Omega t) + F_2(a_1, b_1, a_2, b_2, \Omega)\sin(\Omega t) = 0, \\ F_3(a_1, b_1, a_2, b_2, \Omega)\cos(\Omega t) + F_4(a_1, b_1, a_2, b_2, \Omega)\sin(\Omega t) = 0, \\ F(a_1, b_1, a_2, b_2, \Omega) = (F_1, F_2, F_3, F_4)^{\mathrm{T}} = 0. \end{cases} \tag{8}$$

Next, we solve the equations by the pseudo-arc-length continuation method. The displacement amplitude is expressed as

$$A_{x_1} = \sqrt{a_1^2 + b_1^2}, \quad A_{x_2} = \sqrt{a_2^2 + b_2^2}, \tag{9}$$

and the results are verified with the RK method. The parameters used in the analysis are based on Ref. [49], and are shown in Table 1. The calculation results of the first two sets of parameters show that the analytical and numerical solutions of the x_1 and x_2 transmissibility-frequency curves are in good agreement. The rightward bending of the displacement transmissibility-frequency curve observed in Fig. 2(c) is a characteristic feature of nonlinear systems known as stiffness hardening.

Table 1 The first group of parameters

Parameter	ζ_1	ζ_2	κ	μ	A	L
Figures 2(a) and 2(b)	0.007 3	0.025 9	71	0.1	0.002 5	0.1
Figures 2(c) and 2(d)	0.007 3	0.025 9	110	1	0.005	0.5

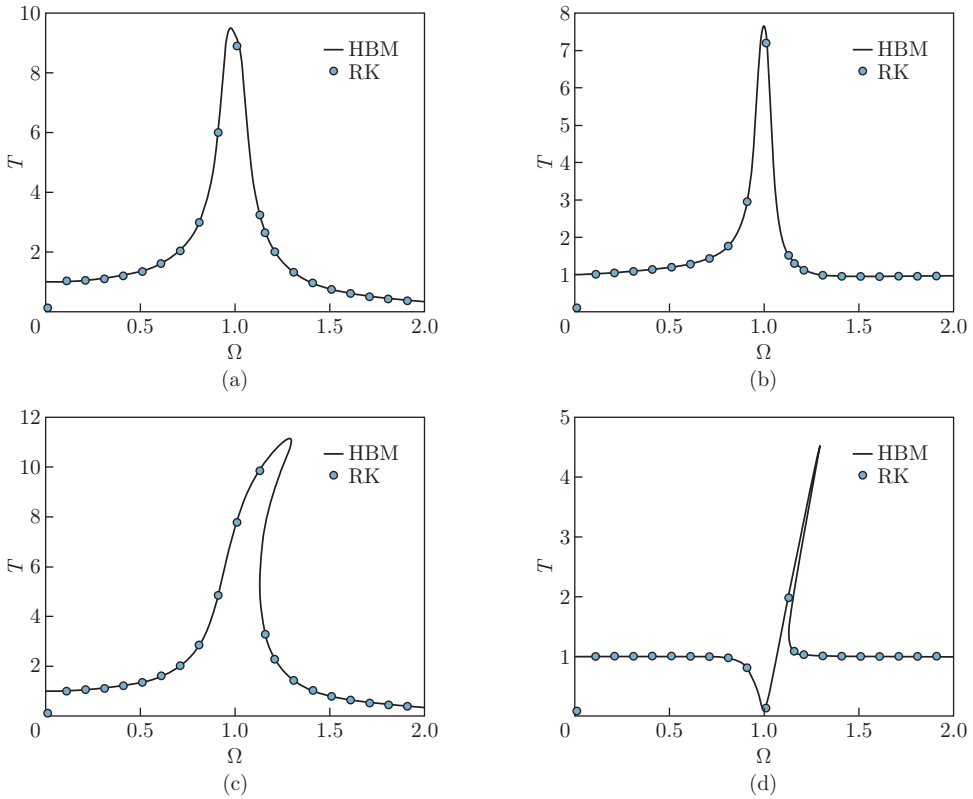

Fig. 2 Comparison of results obtained by the HBM and the RK method with the parameters listed in Table 1: (a) and (c) magnitudes of the relative transmissibility of x_1; (b) and (d) magnitudes of the relative transmissibility of x_2 (color online)

4 Vibration isolation performance and dynamic analysis

To verify the vibration suppression performance of the NI-INES, a comparison is made with a single-degree-of-freedom (SDOF) passive isolator of the same primary mass as the NI-INES. The system parameters are shown in Table 2.

Table 2 The second group of parameters

Parameter	ζ_1	ζ_2	κ	μ	A	L
Value	0.007 3	0.025 9	110	0.1	0.002 5	0.1

Figure 3 shows the results of the the transmissibility-frequency responses and time-displacement curves in different systems and the wavelet transform spectrum of the NI-INES with the parameters listed in Table 2. From Fig. 3(a), it can be seen that the vibration near the resonance frequency of the system is effectively reduced. This can also be seen in Fig. 3(b), where the difference in the amplitude between the SDOF passive isolator and the NI-INES system becomes more pronounced as time increases when the excitation frequency of the external force is the same as the natural frequency of the system. Eventually, the vibration of the NI-INES system reaches a steady state, and is quasi-periodic, enhancing the energy dissipation of the INES. The wavelet transform spectrum of the NI-INES system is shown in Fig. 3(c), which reveals the dominant frequency of vibration. Overall, the system exhibits good vibration suppression performance. The non-dimensional equation of the SDOF passive isolator is as follows:

$$\ddot{x}_1 = -(x_1 - x_e) - 2\zeta_1(\dot{x}_1 - \dot{x}_e). \tag{10}$$

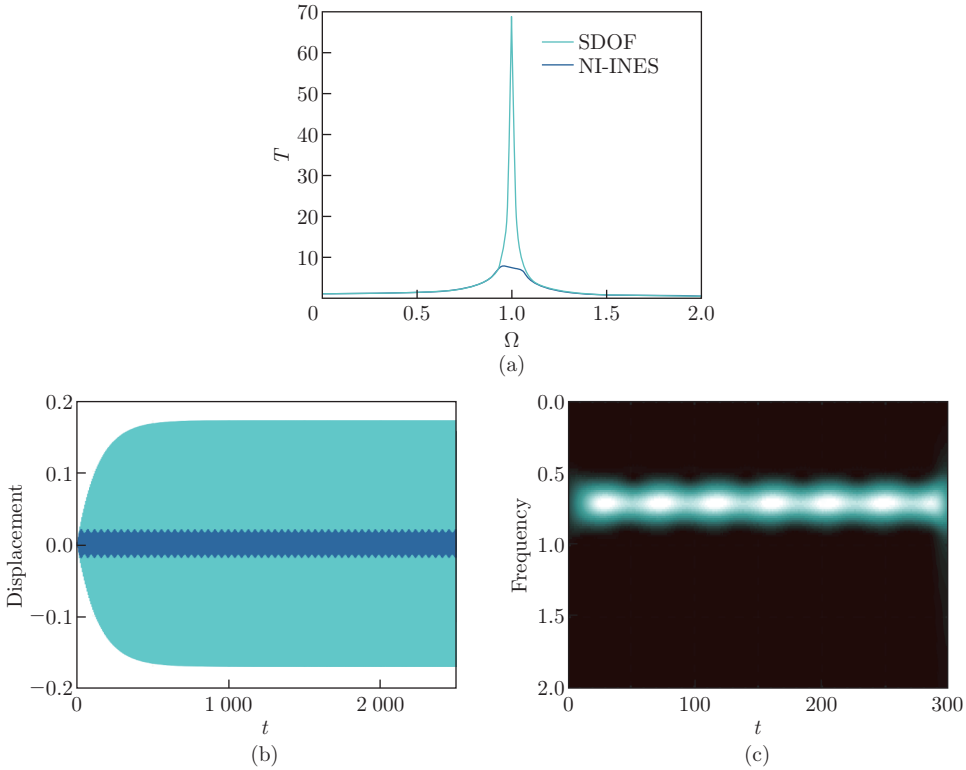

Fig. 3 (a) Comparison of the transmissibility-frequency responses in different systems. (b) Time-displacement curves in different systems, where the blue-green line and grayish blue line represent the SDOF and NI-INES, respectively. (c) Wavelet transform spectrum of the NI-INES (color online)

Based on Table 2, the NI-INES system is studied, and the obtained results are shown in Fig. 4. Figure 4(a) shows that the peak of the displacement transmissibility gradually decreases with the increase in the main structure damping, which is consistent with our expectations. Figure 4(b) shows that the peak of the displacement transmissibility gradually increases with the increase in ζ_2, which is opposite to the case of ζ_1 that we have discussed. For the INES damping, bigger is not always better. It can be seen from Fig. 4(b) that the resonance peak of the system near the intrinsic frequency bends downward when $\zeta_2 = 0.017$, and the dynamic behavior becomes more complicated and the displacement transmissibility-frequency graph undergoes the knotting phenomenon when ζ_2 is further reduced to 0.01. Meanwhile, the system transitions from the steady state to the unstable state. The formation of a knot indicates that the vibrating system is in a non-stationary state, and any small change in its state may lead to an extreme response when the system is very sensitive to the changes in the parameters. Figure 4(c) shows that the displacement transmissibility-frequency response curve of the system shows a decreasing trend when the stiffness ratio increases. When κ increases to 300, the system has a sharp peak near $\Omega = 0.925$ and a protruding peak on the right side near $\Omega = 0.9$. Meanwhile, the system is in an unstable state, and the resonance peak shows a tendency to move to the left when the stiffness ratio increases. In Fig. 4(d), when the inertia coefficient of the inerter is very small, e.g., $\mu = 0.01$, the system is close to the SDOF passive isolator, and the INES loses the role of energy absorption. When $\mu = 0.1$, the system has the best vibration suppression effect. With the increase in μ, the vibration suppression effect of the system decreases, indicating that there is an optimal value of the ratio of the inertia coefficient to the main mass of the system. After obtaining a larger value of μ, the inertia coefficient is several times larger than

the main mass. Although the inertia coefficient is larger, the total mass is still smaller owing to the characteristics of the inertia vessel itself. When $\mu = 10$, we can see that the displacement transmissibility-frequency response curve bends to the left, and the resonance region is more significantly suppressed. In Fig. 4(e), as the excitation amplitude A increases, the displacement transmissibility-frequency response curve shows the same trend as in Fig. 4(c). Initially, as the excitation amplitude A increases, the displacement transmissibility-frequency response curve gradually decreases. When $A = 0.004$, the system undergoes a sudden mutation near $\Omega = 0.925$, and the displacement transmissibility increases significantly. At this time, the system is in an unstable state. As the excitation amplitude A increases, the resonance peak gradually moves to the left.

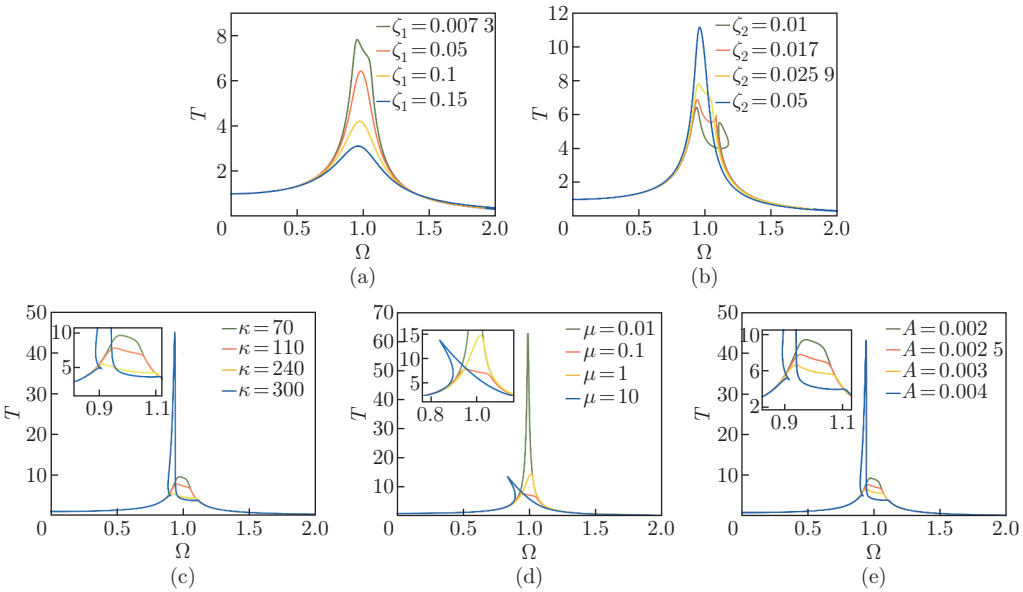

Fig. 4 Transmissibility-frequency responses under fixed parameters in Table 2 except variable ζ_1 (a), variable ζ_2 (b), variable κ (c), variable μ (d), and variable A (e) (color online)

From Fig. 4(d), it can be seen that when μ is taken to be larger, there is an interesting phenomenon that the displacement transmissibility-frequency curve bends to the left. To conduct a parametric study of the NI-INES system with different parameters, μ is set to 15, while the other parameters remain the same as in Table 2. In Fig. 5(a), when the damping of the primary mass is small, the displacement transmissibility-frequency curve bends to the left, and knotting occurs. The vibration suppression effect is not outstanding at this time, but as the damping is further increased, the vibration suppression effect gradually strengthens and the knotting phenomenon disappears. The peak of the curve is not at the natural frequency of the system, but on its left side. When ζ_1 is 0.3, the value of the displacement transmissibility ratio is less than 2, indicating a good vibration suppression effect. In Fig. 5(b), as the damping of the INES increases, the displacement transmissibility-frequency curve shows a similar situation to that in Fig. 5(a). When the damping is small, the curve bends to the left, and knotting occurs around $\Omega = 0.8$. As ζ_2 increases, the peak gradually decreases. When ζ_2 is 0.1, the knotting phenomenon disappears, and the system tends to be stable. Figure 5(c) explores the effect of stiffness on the system. It can be seen from the figure that as the nonlinear stiffness increases, the peak of the displacement transmissibility-frequency curve gradually increases, and the system's resonance peak moves from the left of the natural frequency to the right. The knotting node gradually moves to the right, and the knotting ring shrinks. Figure 5(d) shows

that the main reason for the leftward bending of the displacement transmissibility-frequency curve is the value of μ. The larger the value of μ is, the greater the curvature of the curve moves to the left, and the more knotting occurs. In Fig. 5(e), as the excitation amplitude A increases, the peak of the curve gradually moves to the right and decreases. When A is 0.03, the peak of the curve rises, and a larger knotting ring is produced. It can be noted that near the natural frequency, the displacement transmission ratio is less than 1, and near $\Omega = 0.13$, the displacement transmission ratio is close to 0, indicating that most of the internal energy of the system is dissipated by damping and that there is only a small amount of kinetic energy at the primary mass.

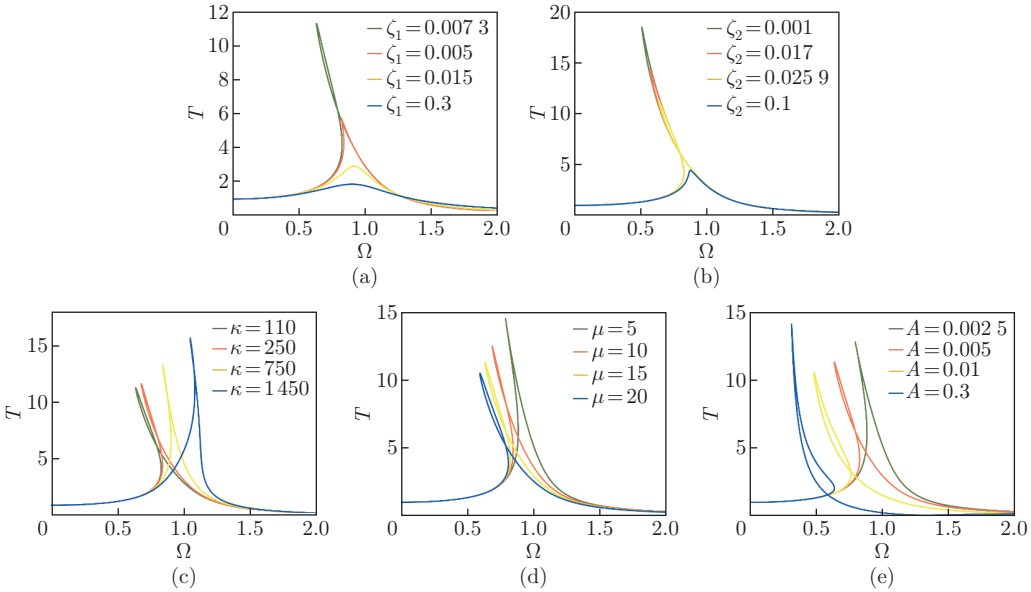

Fig. 5 Transmissibility-frequency responses under fixed parameters in Table 2 except $\mu = 15$ and variable ζ_1 (a), $\mu = 15$ and variable ζ_2 (b), $\mu = 15$ and variable κ (c), variable μ (d), and $\mu = 15$ and variable A (e) (color online)

Then, more complex dynamical phenomena are investigated, where parameters listed in Table 2 are adopted except $\mu = 1$ and $L = 0.5$, and the results are shown in Figs. 6–8. Figure 6 shows the bifurcation diagram of the main structure with respect to the excitation A, Fig. 7 shows the time domain plots and the amplitude spectra, and Fig. 8 shows the phase portraits and the Poincaré maps. In Figs. 6–8, the initial perturbations $\Delta x_1(0)$, $\Delta x_2(0)$, $\Delta \dot{x}_1(0)$, and $\Delta \dot{x}_2(0)$ are 0 at the moment $t = 0$ unless otherwise states.

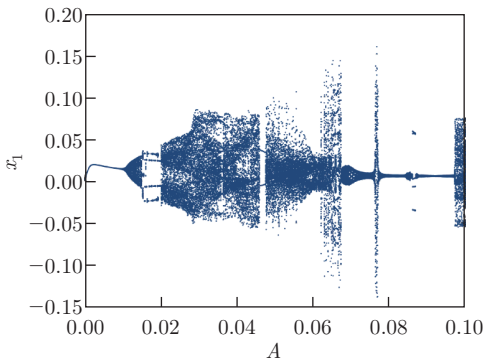

Fig. 6 Global bifurcation chart with external excitation (color online)

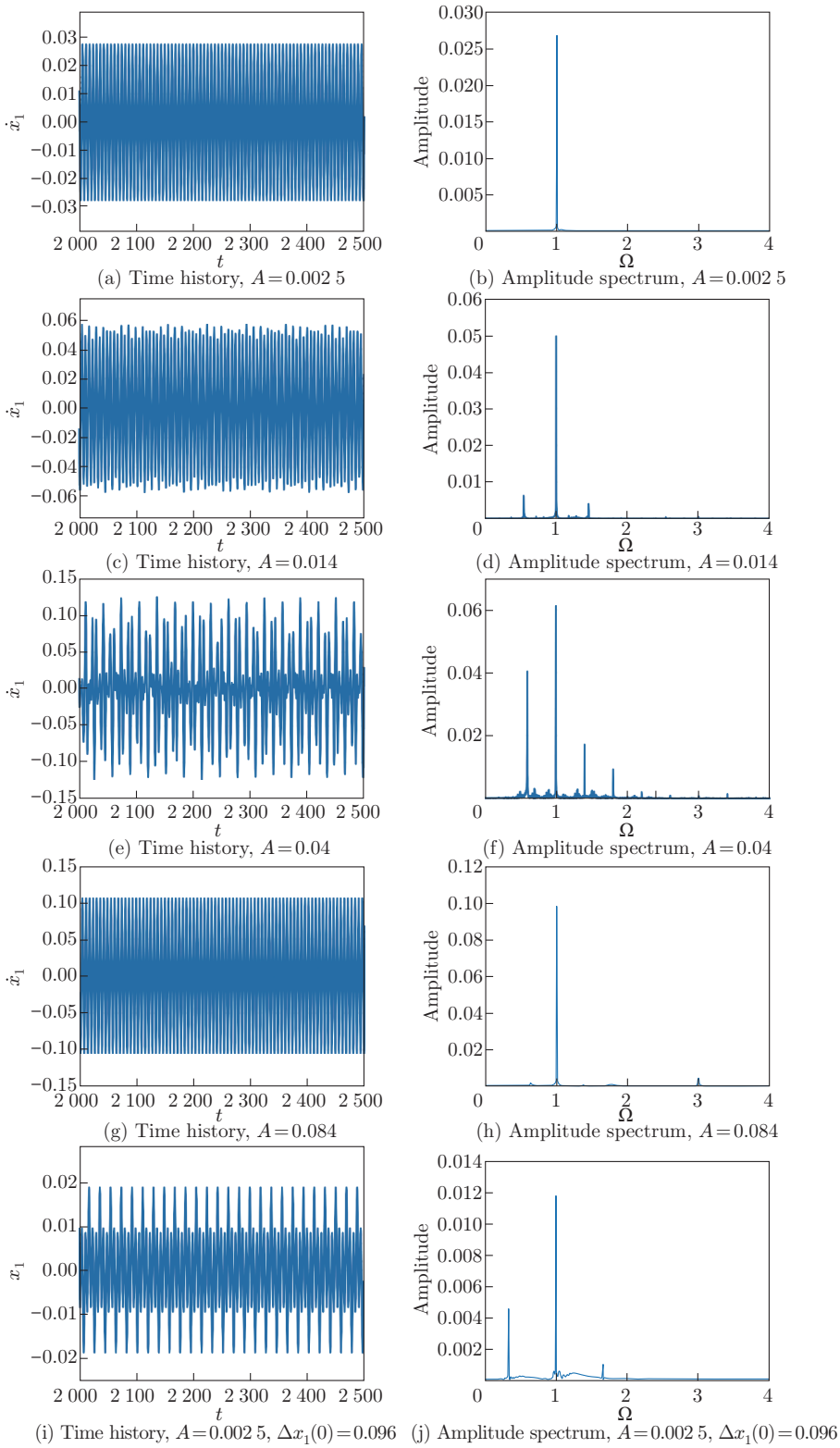

(a) Time history, $A=0.002\,5$ (b) Amplitude spectrum, $A=0.002\,5$

(c) Time history, $A=0.014$ (d) Amplitude spectrum, $A=0.014$

(e) Time history, $A=0.04$ (f) Amplitude spectrum, $A=0.04$

(g) Time history, $A=0.084$ (h) Amplitude spectrum, $A=0.084$

(i) Time history, $A=0.002\,5$, $\Delta x_1(0)=0.096$ (j) Amplitude spectrum, $A=0.002\,5$, $\Delta x_1(0)=0.096$

Fig. 7 Results of the time history and amplitude spectrum under different parameters (color online)

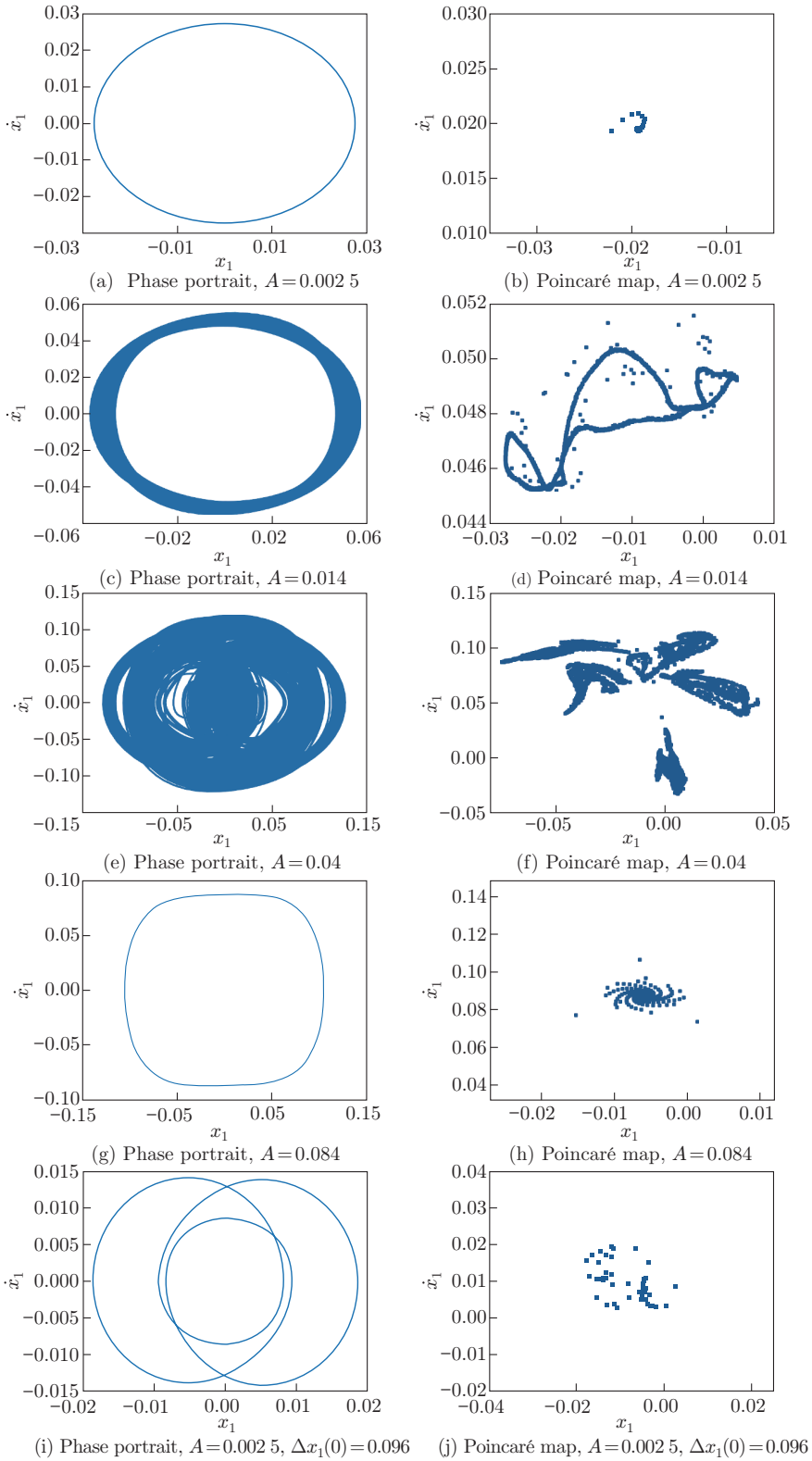

(a) Phase portrait, $A=0.002\,5$ (b) Poincaré map, $A=0.002\,5$

(c) Phase portrait, $A=0.014$ (d) Poincaré map, $A=0.014$

(e) Phase portrait, $A=0.04$ (f) Poincaré map, $A=0.04$

(g) Phase portrait, $A=0.084$ (h) Poincaré map, $A=0.084$

(i) Phase portrait, $A=0.002\,5$, $\Delta x_1(0)=0.096$ (j) Poincaré map, $A=0.002\,5$, $\Delta x_1(0)=0.096$

Fig. 8 Results of the phase portrait and Poincaré map under different parameters (color online)

From Fig. 6, it can be seen that the system is stable when the excitation amplitude is small, and the stability of the system changes as the excitation amplitude A increases. Figures 7 and 8 show that the system exhibits a steady periodic motion with a main frequency of 1 when $A = 0.002\,5$, transitions from a steady periodic motion to a chaotic motion when $A = 0.014$ (indicating bifurcation behavior), and exhibits a more apparent chaotic motion when $A = 0.04$. From Fig. 7, it can also be seen that there is a strongly modulated response, and the system's vibration exhibits more frequency superposition. The complexity of the motion can also be observed from the phase portrait (see Fig. 8). This vibration mode is more conducive to dissipating damping energy and improving system efficiency. When the excitation amplitude further increases, e.g., $A = 0.084$, the system transitions back from chaotic motion to steady periodic motion. Comparing Figs. 7(a), 7(b), 8(a), and 8(b) with Figs. 7(i), 7(j), 8(i), and 8(j), we can note that a perturbation of $\Delta x_1(0) = 0.096$ added to the mass causes the system to transition from a steady periodic motion to a quasi-periodic motion, which is a characteristic instability of nonlinear systems. This indicates that small differences in the initial conditions can lead to large-scale differences in the results.

5 Energy analysis

The analysis of energy flow plays a crucial role in vibration isolation systems. By changing the system parameters, the optimal value of energy absorption by the energy sink in the NI-INES system can be investigated. The energy existing in the main structure will also be greatly reduced when the majority of the damping in the energy sink is dissipated, which will improve the vibration suppression effect. The following formula can be used to describe energy:

$$W_{\text{in}} = T_1 + V_1 + W_1 + V_2 + W_2 + W_{\text{b1}} + W_{\text{b2}}, \tag{11}$$

where W_{in} represents the energy possessed by the NI-INES system at a certain moment. T_1 refers to the kinetic energy of the main mass, V_1 is the potential energy of the main structure spring, and W_1 is the energy consumed by the main structure damping. Similarly, V_2 and W_2 are the spring potential energy and the damping energy consumed by the INES, respectively. W_{b1} represents the energy of the two horizontally arranged NIs, while W_{b2} is the energy of the vertically arranged inerter. Inerters are not energy dissipating components, so they can only temporarily store energy. The expressions for each part are shown as follows:

$$\begin{cases} T_1 = \dfrac{1}{2}\dot{x}_1^2, \quad V_1 = \dfrac{1}{2}(x_1 - A\cos(\Omega t))^2, \quad W_1 = \displaystyle\int_0^t \zeta_1(\dot{x}_1 + \Omega A\sin(\Omega t))^2 \mathrm{d}t, \\ V_2 = \dfrac{1}{4}k(x_2 - x_1)^4, \quad W_2 = \displaystyle\int_0^t \zeta_2(\dot{x}_2 - \dot{x}_1)^2 \mathrm{d}t, \\ W_{\text{b1}} = \dfrac{1}{2}\mu(\dot{x}_2 - \dot{x}_1)^2 \dfrac{(x_2 - x_1)^2}{L^2 + (x_2 - x_1)^2}, \quad W_{\text{b2}} = \dfrac{1}{2}\mu(\dot{x}_2 - \dot{x}_1)^2. \end{cases} \tag{12}$$

In order to investigate the absorption capability of the additional structural energy sink, we define the absorption efficiency of the energy sink as

$$\eta = \frac{W_2}{W_{\text{in}}} \times 100\%,$$

where W_{in} represents the input energy. The three-dimensional and two-dimensional plots in Fig. 9 are calculated by using the parameters listed in Table 2. From Fig. 9(a), it can be seen that the damping dissipation energy of the INES changes significantly with both the inertia ratio μ and the excitation amplitude A. However, it can be observed that the INES exhibits a

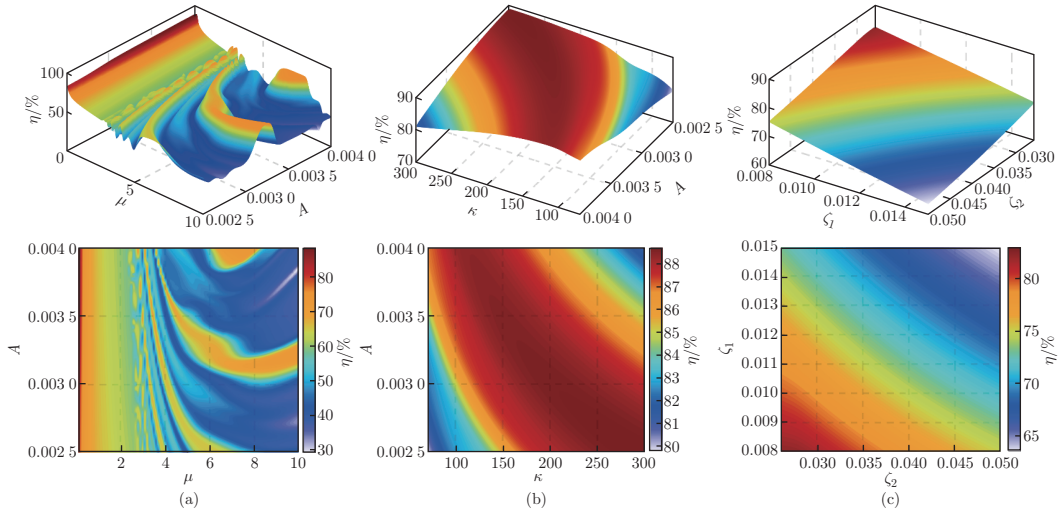

Fig. 9 Diagrams of energy absorbed in the INES under fixed parameters in Table 2 except variable μ and A (a), variable κ and A (b), and variable ζ_1 and ζ_2 (c) (color online)

good energy absorption efficiency when μ is small and within a given range of A, which greatly reduces the energy present in the main structure and plays a role in absorbing vibrations. As μ increases, the energy absorption efficiency decreases, and a wavy pattern appears. In some blue regions, the efficiency of the energy sink is very low. In Fig. 9(b), the areas with good energy absorption are mainly distributed along the diagonal line. The efficiency η in most regions is above 80%, which is related to the small values of μ in Table 2 and is consistent with the phenomenon in Fig. 9(a). In Fig. 9(c), the areas with good performance are concentrated in the direction where ζ_1 and ζ_2 are small. As ζ_1 and ζ_2 increase, η decreases along the sloping direction. Therefore, it is not better to take a larger value of damping, and there should be a more reasonable range.

It can be seen from Fig. 9 that the value of μ has a large effect on the effect of energy absorption in the energy sink. Based on the parameters in Table 2, a multiparametric analysis is performed under the condition where $\mu = 1$, $A = 0.005$, $L = 0.5$, and the rest of the parameters are consistent with those in Fig. 9. In Fig. 10(a), it can be seen that when μ is small, there is a peak in the range of 0–5. Initially, as μ increases, the energy absorption efficiency of the energy sink rises rapidly from about 10% to about 90% and then decreases slowly. When the value of μ is larger, the energy absorption efficiency of the energy sink stays at a low level. It can be seen that there is an optimal value of μ for this set of parameters. In Fig. 10(b), when the excitation amplitude A takes a small value, it can be seen that the energy absorption efficiency is below 70%. With the increase in A and the change in κ, the fluctuation of the energy absorption rate is more complicated, and the overall maintains at about 80%. However, there are some blue points in the distribution with lower absorption efficiency. From Fig. 10(b), it can also be seen that there is also a more stable semi-ring-shaped region for the energy absorption rate. In Fig. 10(c), it can be seen that the absorption efficiency of the energy sink is good when ζ_1 is small and ζ_2 is large. As ζ_1 increases while ζ_2 decreases, the energy absorption rate decreases along the slope direction. It can be found that the energy absorption rate is lower when ζ_2 is small, regardless of the value of ζ_1.

6 Conclusions

This paper proposes a new isolator, i.e., NI-INES. The movement of the vibration isolator is predicted by using the RK method and the HBM. The vibration suppression of the system

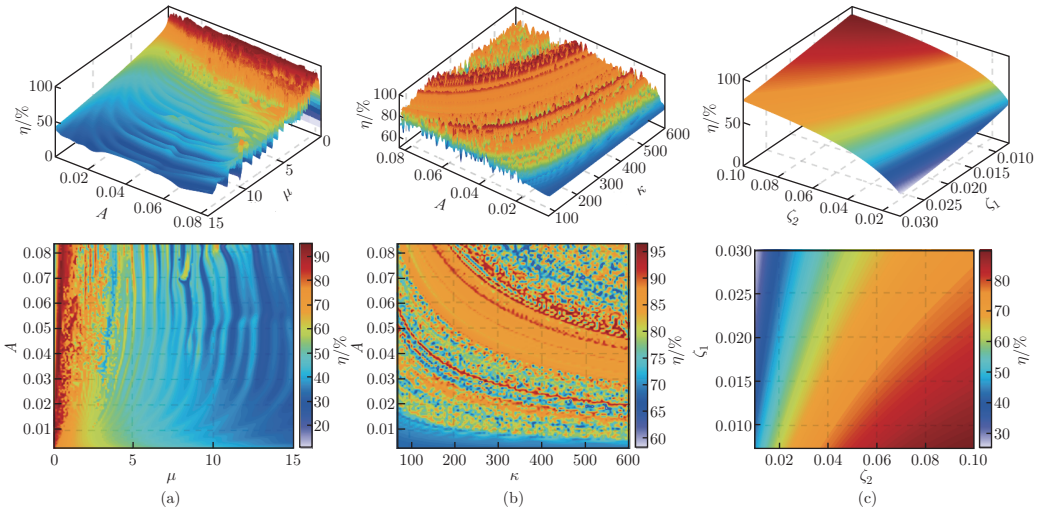

Fig. 10 Diagrams of energy absorbed in the INES under fixed parameters in Table 2 except variable μ and A (a); $\mu = 1$, $L = 0.5$, and variable κ and A (b); and $\mu = 1$, $A = 0.005$, $L = 0.5$, and variable ζ_1 and ζ_2 (c) (color online)

is evaluated by using the displacement transmissibility, and is compared with a conventional SDOF vibration suppression device. A better vibration suppression effect can be seen from the transmissibility-frequency response plot and the time-domain plot. By changing the parameters of the system, multiple sets of transmissibility-frequency response analyses are performed on the system. It can be seen that when the coefficient of the inerter is taken to be larger, the phenomenon of softening stiffness occurs, and the curve bends toward the low frequency region. At the intrinsic frequency of the system, the effect of the excitation amplitude on the dynamics of the system is investigated. As the excitation amplitude increases, the vibration of the main structure changes from steady-state periodic motion to chaotic motion, and bifurcation behavior is expected to occur. The system is very sensitive to the initial conditions, which is an important sign of a nonlinear system. Finally, several sets of energy analyses on the system parameters are carried out to investigate the efficiency of the INES in absorbing energy and to give better parameter intervals. To summarize the results of this paper, the complex dynamical behavior of the new NI-INES structure is investigated, and the preferred parameter interval for energy absorption in NESs is analyzed from the energy point of view. This study provides new insights into the design of vibration isolation.

Conflict of interest Linqun CHEN is an editorial board member for *Applied Mathematics and Mechanics* (*English Edition*) and was not involved in the editorial review or the decision to publish this article. The authors declare no conflict of interest.

Availability of data and materials The datasets used or analyzed during the current study are available from the corresponding author on reasonable request.

References

[1] GRIFFIN, M. J. *Handbook of Human Vibration*, Academic Press, Pittsburgh (1990)

[2] CUI, J. G., YANG, T. Z., NIU, M. Q., and CHEN, L. Q. Tunable roton-like dispersion relation with parametric excitations. *Journal of Applied Mechanics*, **89**(11), 111005 (2022)

[3] CUI, J. G., YANG, T. Z., NIU, M. Q., and CHEN, L. Q. Interaction effects of driving amplitudes

and frequencies on transitivity in a granular chain. *Journal of Sound and Vibration*, **529**, 116966 (2022)

[4] CUI, J. G., NIU, M. Q., CHEN, L. Q., and YANG, T. Z. Asymmetric propagation of acoustic waves in a conical granular chain. *Communications in Nonlinear Science and Numerical Simulation*, **116**, 106885 (2023)

[5] HOUSNER, G. W., BERGMAN, L. A., CAUGHEY, T. K., CHASSIAKOS, A. G., CLAUS, R. O., MASRI, S. F., SKELTON, R. E., SOONG, T. T., SPENCER, B. F., and YAO, J. T. P. Structural control: past, present, and future. *Journal of Engineering Mechanics*, **123**(9), 897–971 (1997)

[6] TIGLI, O. F. Optimum vibration absorber (tuned mass damper) design for linear damped systems subjected to random loads. *Journal of Sound and Vibration*, **331**(13), 3035–3049 (2012)

[7] IGUSA, T. and XU, K. Vibration control using multiple tuned mass dampers. *Journal of Sound and Vibration*, **175**(4), 491–503 (1994)

[8] ZUO, L. and NAYFEH, S. A. The two-degree-of-freedom tuned-mass damper for suppression of single-mode vibration under random and harmonic excitation. *Journal of Vibration and Acoustics*, **128**(1), 56–65 (2006)

[9] NAGASHIMA, I. and SHINOZAKI, Y. Variable gain feedback control technique of active mass damper and its application to hybrid structural control. *Earthquake Engineering and Structural Dynamics*, **26**, 815–838 (1997)

[10] LOH, C. and LIN, P. Kalman filter approach for the control of seismic-induced building vibration using active mass damper systems. *Structural Design of Tall and Special Buildings*, **6**, 209–224 (1997)

[11] YANG, T. Z., DUAN, Z. L., MENG, X. B., LIU, S. L., and CHEN, L. Q. Roton-enabled mechanical diode at extremely low frequency. *Journal of Applied Mechanics*, **91**(1), 011010 (2024)

[12] CARRELLA, A., BRENNAN, M. J., and WATERS, T. P. Static analysis of a passive vibration isolator with quasi-zero-stiffness characteristic. *Journal of Sound and Vibration*, **301**(3-5), 678–689 (2007)

[13] ROBERSON, R. E. Synthesis of a nonlinear dynamic vibration absorber. *Journal of the Franklin Institute*, **254**(3), 205–220 (1952)

[14] ZHAO, F., JI, J., YE, K., and LUO, Q. An innovative quasi-zero stiffness isolator with three pairs of oblique springs. *International Journal of Mechanical Sciences*, **192**, 106093 (2021)

[15] YE, K., JI, J. C., and BROWN, T. Design of a quasi-zero stiffness isolation system for supporting different loads. *Journal of Sound and Vibration*, **471**, 115198 (2020)

[16] GENDELMAN, O. V., MANEVITCH, L. I., VAKAKIS, A. F., and M'CLOSKEY, R. Energy pumping in nonlinear mechanical oscillators: part I, dynamics of the underlying Hamiltonian systems. *Journal of Applied Mechanics*, **68**(1), 34–41 (2001)

[17] VAKAKIS, A. F. and GENDELMAN, O. V. Energy pumping in nonlinear mechanical oscillators: part II, resonance capture. *Journal of Applied Mechanics*, **68**(1), 42–48 (2001)

[18] LEE, Y. S., VAKAKIS, A. F., BERGMAN, L. A., MCFARLAND, D. M., KERSCHEN, G., NUCERA, F., TSAKIRTZIS, S., and PANAGOPOULOS, P. N. Passive non-linear targeted energy transfer and its applications to vibration absorption: a review. *Proceedings of the Institution of Mechanical Engineers, Part K: Journal of Multi-body Dynamics*, **222**(2), 77–134 (2008)

[19] VAKAKIS, A. F., GENDELMAN, O. V., BERGMAN, L. A., MCFARLAND, D. M., KERSCHEN, G., and LEE, Y. S. *Nonlinear Targeted Energy Transfer in Mechanical and Structural Systems*, Springer, Berlin (2008)

[20] LU, Z., YANG, T., BRENNAN, M. J., LI, X., and LIU, Z. G. On the performance of a two-stage vibration isolation system which has geometrically nonlinear stiffness. *Journal of Vibration and Acoustics*, **136**(6), 064501 (2014)

[21] LU, Z. Q., BRENNAN, M. J., YANG, T. J., LI, X. H., and LIU, Z. G. An investigation of a two-stage nonlinear vibration isolation system. *Journal of Sound and Vibration*, **332**(6), 1456–1464 (2013)

[22] GENDELMAN, O. V., EMMANUEL, G., and LAMARQUE, C. H. Quasiperiodic energy pumping in coupled oscillators under periodic forcing. *Journal of Sound and Vibration*, **294**(4-5), 651–662 (2006)

[23] TRIPATHI, A., GROVER, P., and KALMÁR-NAGY, T. On optimal performance of nonlinear energy sinks in multiple-degree-of-freedom systems. *Journal of Sound and Vibration*, **388**, 272–297 (2017)

[24] GOURDON, E. and LAMARQUE, C. Nonlinear energy sink with uncertain parameters. *Journal of Computational and Nonlinear Dynamics*, **1**(3), 187–195 (2006)

[25] ZANG, J., YUAN, T. C., LU, Z. Q., ZHANG, Y. W., DING, H., and CHEN, L. Q. A lever-type nonlinear energy sink. *Journal of Sound and Vibration*, **437**, 119–134 (2018)

[26] GENG, X. F., DING, H., MAO, X. Y., and CHEN, L. Q. Nonlinear energy sink with limited vibration amplitude. *Mechanical Systems and Signal Processing*, **156**, 107625 (2021)

[27] DANG, W. H., WANG, Z. H., CHEN, L. Q., and YANG, T. Z. A high-efficient nonlinear energy sink with a one-way energy converter. *Nonlinear Dynamics*, **109**, 2247–2261 (2022)

[28] SAVADKOOHI, A. T., LAMARQUE, C. H., and DIMITRIJEVIC, Z. Vibratory energy exchange between a linear and a nonsmooth system in the presence of the gravity. *Nonlinear Dynamics*, **70**, 1473–1483 (2012)

[29] LAMARQUE, C. H., GENDELMAN, O. V., SAVADKOOHI, A. T., and ETCHEVERRIA, E. Targeted energy transfer in mechanical systems by means of non-smooth nonlinear energy sink. *Acta Mechanica*, **221**, 175–200 (2011)

[30] GEORGIADIS, F., VAKAKIS, A. F., MCFARLAND, D. M., and BERGMAN, L. Shock isolation through passive energy pumping caused by nonsmooth nonlinearities. *International Journal of Bifurcation and Chaos*, **15**, 1989–2001 (2005)

[31] WIERSCHEM, N. E., HUBBARD, S. A., LUO, J., FAHNESTOCK, L. A., SPENCER, B. F., MCFARLAND, D. M., QUINN, D. D., VAKAKIS, A. F., and BERGMAN, L. A. Response attenuation in a large-scale structure subjected to blast excitation utilizing a system of essentially nonlinear vibration absorbers. *Journal of Sound and Vibration*, **389**, 52–72 (2017)

[32] LUO, J., WIERSCHEM, N. E., HUBBARD, S. A., FAHNESTOCK, L. A., QUINN, D. D., MCFARLAND, D. M., SPENCER, B. F., VAKAKIS, A. F., and BERGMAN, L. A. Large-scale experimental evaluation and numerical simulation of a system of nonlinear energy sinks for seismic mitigation. *Engineering Structures*, **77**, 34–48 (2014)

[33] NUCERA, F., VAKAKIS, A. F., MCFARLAND, D. M., BERGMAN, L. A., and KERSCHEN, G. Targeted energy transfers in vibro-impact oscillators for seismic mitigation. *Nonlinear Dynamics*, **50**, 651–677 (2007)

[34] GOURC, E., SEGUY, S., MICHON, G., BERLIOZ, A., and MANN, B. P. Quenching chatter instability in turning process with a vibro-impact nonlinear energy sink. *Journal of Sound and Vibration*, **355**, 392–406 (2015)

[35] BAB, S., KHADEM, S. E., SHAHGHOLI, M., and ABBASI, A. Vibration attenuation of a continuous rotor-blisk-journal bearing system employing smooth nonlinear energy sinks. *Mechanical Systems and Signal Processing*, **84**, 128–157 (2017)

[36] LEE, Y. S., VAKAKIS, A. F., BERGMAN, L. A., MCFARLAND, D. M., and KERSCHEN, G. Suppression aeroelastic instability using broadband passive targeted energy transfers, part 1: theory. *AIAA Journal*, **45**(3), 693-711(2007)

[37] LEE, Y. S., KERSCHEN, G., MCFARLAND, D. M., HILL, W. J., NICHKAWDE, C., STRGANAC, T. W., BERGMAN, L. A., and VAKAKIS, A. F. Suppressing aeroelastic instability using broad band passive targeted energy transfers, part 2: experiments. *AIAA Journal*, **45**(10), 2391–2400 (2007)

[38] ZHANG, Y. W., LU, Y. N., and CHEN, L. Q. Energy harvesting via nonlinear energy sink for whole-spacecraft. *Science China Technological Sciences*, **62**, 1483–1491 (2019)

[39] YANG, T. Z., LIU, T., TANG, Y., HOU, S., and LV, X. F. Enhanced targeted energy transfer for adaptive vibration suppression of pipes conveying fluid. *Nonlinear Dynamics*, **97**, 1937–1944 (2018)

[40] SUN, Y. H., ZHANG, Y. W., DING, H., and CHEN, L. Q. Nonlinear energy sink for a flywheel system vibration reduction. *Journal of Sound and Vibration*, **429**, 305–324 (2018)

[41] CHEN, L. Q., ZHANG, G. C., and DING, H. Internal resonance in forced vibration of coupled cantilevers subjected to magnetic interaction. *Journal of Sound and Vibration*, **354**, 196–218 (2015)

[42] CHEN, H. Y., DING, H., LI, S. H., and CHEN, L. Q. Convergent term of the Galerkin truncation for dynamic response of sandwich beams on nonlinear foundations. *Journal of Sound and Vibration*, **483**, 115514 (2020)

[43] FANG, Z. W., ZHANG, Y. W., LI, X., DING, H., and CHEN, L. Q. Integration of a nonlinear energy sink and a giant magnetostrictive energy harvester. *Journal of Sound and Vibration*, **391**, 35–49 (2017)

[44] MANN, B. P. and SIMS, N. D. Energy harvesting from the nonlinear oscillations of magnetic levitation. *Journal of Sound and Vibration*, **319**(1-2), 515–530 (2009)

[45] KREMER, D. and LIU, K. F. A nonlinear energy sink with an energy harvester: transient responses. *Journal of Sound and Vibration*, **333**(20), 4859–4880 (2014)

[46] ZHANG, Y., TANG, L., and LIU, K. Piezoelectric energy harvesting with a nonlinear energy sink. *Journal of Intelligent Materials Systems and Structures*, **28**(3), 307–322 (2017)

[47] HAN, Q. K., WANG, T. Y., DING, Z., XU, X. P., and CHU, F. L. Magnetic equivalent modeling of stator currents for localized fault detection of planetary gearboxes coupled to electric motors. *IEEE Transactions on Industrial Informatics*, **68**(3), 2575–2586 (2021)

[48] SMITH, M. C. Synthesis of mechanical networks: the inerter. *IEEE Transactions on Automatic Control*, **47**(10), 1648–1662 (2002)

[49] LAZAR, I. F., NEILD, S. A., and WAGG, D. J. Using an inerter-based device for structural vibration suppression. *Earthquake Engineering & Structural Dynamics*, **43**(8), 1129–1147 (2014)

[50] KUHNERT, W. M., GONCALVES, P. J. P., LEDEZMA-RAMIREZ, D. F., and BRENNAN, M. J. Inerter-like devices used for vibration isolation: a historical perspective. *Journal of the Franklin Institute*, **358**(1), 1070–1086 (2021)

[51] CHEN, M., PAPAGEORGIOU, C., SCHEIBE, F., WANG, F., and SMITH, M. The missing mechanical circuit element. *IEEE Circuits and Systems Magazine*, **9**, 10–26 (2009)

[52] CHILLEMI, M., FURTMÜLLER, T., ADAM, C., and PIRROTTA, A. Nonlinear mechanical model of a fluid inerter. *Mechanical Systems and Signal Processing*, **188**, 109986 (2023)

[53] ZHANG, Z., LU, Z. Q., DING, H., and CHEN, L. Q. An inertial nonlinear energy sink. *Journal of Sound and Vibration*, **450**, 199–213 (2019)

[54] DUAN, Z. L., CUI, J. G., CHEN, L. Q., and YANG, T. Z. Nonlinear mechanical roton. *Journal of Applied Mechanics*, **90**(3), 031010 (2023)

[55] SAPSIS, T. P., QUINN, D. D., VAKAKIS, A. F., and BERGMAN, L. A. Effective stiffening and damping enhancement of structures with strongly nonlinear local attachments. *Journal of Vibration and Acoustics*, **134**(1), 011016 (2012)

[56] MORAES, F. D. H., SILVEIRA, M., and GONÇALVES, P. J. P. On the dynamics of a vibration isolator with geometrically nonlinear inerter. *Nonlinear Dynamics*, **93**, 1325–1340 (2018)

[57] YANG, J., JIANG, J. Z., and NEILD, S. A. Dynamic analysis and performance evaluation of nonlinear inerter-based vibration isolators. *Nonlinear Dynamics*, **99**, 1823–1839 (2020)

[58] DANG, W. H., LIU, S. L., CHEN, L. Q., and YANG, T. Z. A dual-stage inerter-enhanced nonlinear energy sink. *Nonlinear Dynamics*, **111**, 6001–6015 (2023)

[59] DONG, Z., SHI, B., YANG, J., and LI, T. Y. Suppression of vibration transmission in coupled systems with an inerter-based nonlinear joint. *Nonlinear Dynamics*, **107**, 1637–1662 (2022)

[60] SHI, B., DAI, W., and YANG, J. Performance analysis of a nonlinear inerter-based vibration isolator with inerter embedded in a linkage mechanism. *Nonlinear Dynamics*, **109**, 419–442 (2022)